

Contents

1	Introduction and Theory Overview	1
1.1	Introduction	1
1.2	Theory Overview	2
1.2.1	Heavy Vector Triplet Model	2
1.2.2	Basic Phenomenology	3
1.2.3	Explicit Models	8
2	CMS detector and LHC	11
2.1	Large Hadron Collider	11
2.2	Compact Muon Solenoid	13
2.2.1	Tracker	15
2.2.2	ECAL	16
2.2.3	HCAL	17
2.2.4	Muon Chamber	17
2.2.5	Trigger System	17

List of Figures

1-1	Branching ratios as a function of the resonance mass for the HVT benchmark model A(left) and model B(right).	10
1-2	Theoretical production cross-section as a function of new resonance particles for HVT model B benchmark. Dash lines are 8 TeV predictions while solid lines are 13 TeV predictions.	10
2-1	Overview of the LHC and relative location of the detectors.	12
2-2	CERN accelerator complex.	13
2-3	Structure overview of the CMS detector.	14
2-4	Schematic layout of tracker.	15
2-5	The pixel detector inside tracker.	15
2-6	Schematic layout of the CMS ECAL.	17

List of Tables

Chapter 1

Introduction and Theory Overview

1.1 Introduction

This thesis presents the analysis details and the results of the search for heavy resonances decaying into a Z boson and a Higgs boson (h) at the center-of-mass energy of 8 TeV, using 19.7 fb^{-1} p-p collision data. In turn, the Z boson is identified through its leptonic decays (leptons often refer to e and μ only in experiments. $l = e, \mu$). The Higgs boson h is expected to hadronically decay into a pair of b-quarks. The investigated final states consist of two charged leptons which are identified in the detector and limit the presence of the background, and two b-quarks from the hadronic Higgs decay which collects the largest possible fraction of Higgs events.

This thesis is organised as follows. In the latter part of this chapter, the model that predicts heavy resonances is introduced, including the expected cross section and the specification of model parameters. In chapter 2, the LHC and the CMS experiment are described, including the information of each sub-detector and the trigger system of the CMS. The details of the analysis are shown in chapter 3. This chapter reveals the way to reconstruct physical objects in CMS. By adding some proper kinematic selections on those physics objects, the interested events in data collected by the CMS detector can be selected. Moreover, this chapter shows the comparison between data and simulation. In the last chapter, the results of the search and the conclusion are presented.

1.2 Theory Overview

Although the Higgs boson discovered by the ATLAS and CMS collaborations [1–3] imposes strong constraints on theories beyond the Standard Model (SM), the extreme fine tuning in quantum corrections required to have a light fundamental Higgs boson with mass close to 125 GeV [4–7] suggests that the Standard Model may be incomplete, and not valid beyond a scale of a few TeV. Various dynamical electroweak symmetry breaking scenarios which attempt to solve this naturalness problem, such as Minimal Walking Technicolor [8], Little Higgs [9–11], or composite Higgs models [12–14] predict the existence of new resonances decaying to a vector boson plus a Higgs boson.

1.2.1 Heavy Vector Triplet Model

Resonance searches are typically not sensitive to all the details and the free parameters of the underlying model, but only to those parameters or combinations of parameters that control the mass of the resonance and the interactions involved in its production and decay. Therefore, one can employ a simplified description of the resonance defined by a phenomenological Lagrangian where only the relevant couplings and mass parameters are retained. This model-independent strategy applies a Heavy Vector Triplet (HVT) [15] to the Standard Model group and reproduces a large class of explicit models. In Eq. (1.1), the mathematical form of the simplified Lagrangian is defined, where V_ν^a , $a = 1, 2, 3$, is a real vector with vanishing hypercharge in the adjoint representation of $SU(2)_L$, it describes one charged and one neutral heavy spin-1 particle with charge eigenstate fields, and $D_{[\mu}V_{\nu]}^a$ represents the covariant derivative.

$$\begin{aligned} \mathcal{L}_V = & -\frac{1}{4}D_{[\mu}V_{\nu]}^a D^{[\mu}V^{\nu]a} + \frac{m_V^2}{2}V_\mu^a V^{\mu a} \\ & + ig_V c_H V_\mu^a H^\dagger \tau^a \overleftrightarrow{D}^\mu H + \frac{g^2}{g_V} c_F V_\mu^a \sum_f \bar{f}_L \gamma^\mu \tau^a f_L \\ & + \frac{g_V}{2} c_{VVV} \epsilon_{abc} V_\mu^a V_\nu^b D^{[\mu}V^{\nu]c} + \text{quadrilinear terms} \end{aligned} \quad (1.1)$$

$$V_\mu^\pm = \frac{V_\mu^1 \mp iV_\mu^2}{\sqrt{2}}, \quad V_\mu^0 = V_\mu^3 \quad (1.2)$$

$$D_{[\mu}V_{\nu]}^a = D_\mu V_\nu^a - D_\nu V_\mu^a, \quad D_\mu V_\nu^a = \partial_\mu V_\nu^a + g\epsilon^{abc}W_\mu^b V_\nu^c \quad (1.3)$$

$$H = \begin{pmatrix} \phi^+ \\ \phi^- \end{pmatrix} = \begin{pmatrix} \frac{1}{\sqrt{2}}(\phi_1 + i\phi_2) \\ \frac{1}{\sqrt{2}}(\phi_3 + i\phi_4) \end{pmatrix} \quad (1.4)$$

44

45 In these models, new heavy vector bosons (V^\pm, V^0) that couple to the SM Higgs
 46 doublet (Eq. 1.4) and SM gauge bosons with the parameters c_H and g_V and to the
 47 fermions via the combination $(g^2/g_V)c_F$. The parameter g_V represents the strength
 48 of the new vector boson interaction, while c_H and c_F represent the couplings to the
 49 Higgs and the fermions respectively, and are expected to be of the order of unity in
 50 most models.

51 1.2.2 Basic Phenomenology

52 Masses and Mixings

After electro-weak symmetry breaking (EWSB), the only massless state is photon, which can be identified as the gauge field associated with the unbroken $U(1)_{em}$. The two other neutral mass eigenstates are the SM Z boson and one heavy vector of mass M_0 which are obtained by diagonalizing the mass matrix of the (Z, V^0) system by a rotation with angle θ_N

$$\begin{pmatrix} Z \\ V^0 \end{pmatrix} \rightarrow \begin{pmatrix} \cos \theta_N & \sin \theta_N \\ -\sin \theta_N & \cos \theta_N \end{pmatrix} \begin{pmatrix} Z \\ V^0 \end{pmatrix}. \quad (1.5)$$

The mass matrix is

$$\mathcal{M}_N^2 = \begin{pmatrix} \hat{m}_Z^2 & c_H \xi \hat{m}_Z \hat{m}_V \\ c_H \xi \hat{m}_Z \hat{m}_V & \hat{m}_V^2 \end{pmatrix}, \text{ where } \begin{cases} \hat{m}_Z = \frac{e\hat{v}}{2 \sin \theta_W \cos \theta_W} \\ \hat{m}_V^2 = m_V^2 + g_V^2 c_{VVHH} \hat{v}^2 \\ \xi = \frac{g_V \hat{v}}{2 \hat{m}_V} \end{cases} \quad (1.6)$$

In the above equations \hat{v} denotes the Vacuum Expectation Value (VEV) defined by $\langle H^\dagger H \rangle = \hat{v}^2/2$, and one should know the masses \hat{m}_Z and \hat{m}_V do not coincide with the physical Z boson and the masses of the new resonances of this model, although they do in the approximations later. The mass eigenvalues and the rotation angles are easily obtained by inverting the relations

$$\begin{aligned} Tr[\mathcal{M}_N^2] &= \hat{m}_Z^2 + \hat{m}_V^2 = m_Z^2 + M_0^2, \\ Det[\mathcal{M}_N^2] &= \hat{m}_Z^2 \hat{m}_V^2 (1 - c_H^2 \xi^2) = m_Z^2 M_0^2, \\ \tan 2\theta_N &= \frac{2c_H \xi \hat{m}_Z \hat{m}_V}{\hat{m}_V^2 - \hat{m}_Z^2}. \end{aligned} \quad (1.7)$$

53 Notice that the tangent can be uniquely inverted because the angle θ_N is in the range
 54 $[-\pi/4, \pi/4]$ in the parameter region we will be interested in, where $\hat{m}_Z < \hat{m}_V$, and
 55 M_0 represents the real mass eigenvalue of the neutral heavy vector boson.

The situation is similar in the charged vector mass matrix of (W^\pm, V^\pm) system, and M_\pm denotes the real mass eigenvalue of charged states as well.

$$\mathcal{M}_C^2 = \begin{pmatrix} \hat{m}_W^2 & c_H \xi \hat{m}_W \hat{m}_V \\ c_H \xi \hat{m}_W \hat{m}_V & \hat{m}_V^2 \end{pmatrix}, \text{ where } \hat{m}_W = \frac{e\hat{v}}{2 \sin \theta_W} = \cos \theta_W \hat{m}_Z, \quad (1.8)$$

where it is diagonalized by

$$\begin{aligned} Tr[\mathcal{M}_C^2] &= \hat{m}_W^2 + \hat{m}_V^2 = m_W^2 + M_\pm^2, \\ Det[\mathcal{M}_C^2] &= \hat{m}_W^2 \hat{m}_V^2 (1 - c_H^2 \xi^2) = m_W^2 M_\pm^2, \\ \tan 2\theta_C &= \frac{2c_H \xi \hat{m}_W \hat{m}_V}{\hat{m}_V^2 - \hat{m}_W^2}. \end{aligned} \quad (1.9)$$

By checking Eq. (1.6) and Eq. (1.8), the charged and neutral mass matrices are connected by custodial symmetry, which can be shown in full generality to imply

$$\mathcal{M}_C^2 = \begin{pmatrix} \cos \theta_W & 0 \\ 0 & 1 \end{pmatrix} \mathcal{M}_N^2 \begin{pmatrix} \cos \theta_W & 0 \\ 0 & 1 \end{pmatrix} . \quad (1.10)$$

By taking the determinant of the above equation, or equivalently by comparing the charged and neutral determinants in Eq. (1.7) and Eq. (1.9), we obtain a generalized custodial relation among the physical masses

$$m_W^2 M_\pm^2 = \cos^2 \theta_W m_Z^2 M_0^2 . \quad (1.11)$$

From the simple formula above, we can start to identify the physically reasonable region of the parameter space in this model. We aim at describing new vectors with masses at or above the TeV scale, but we also want the SM masses $m_{W,Z} \sim 100$ GeV to be reproduced. Therefore we require a hierarchy in the mass relation of SM Z and W bosons versus the new vectors.

$$\frac{\hat{m}_{W,Z}}{\hat{m}_V} \sim \frac{m_{W,Z}}{M_{\pm,0}} \leq 10^{-1} \ll 1 \quad (1.12)$$

In the limit of Eq. (1.12) we obtain simple approximation for m_W and m_Z

$$\begin{aligned} m_Z^2 &= \hat{m}_Z^2 (1 - c_H^2 \xi^2) (1 + \mathcal{O}(\hat{m}_Z^2 / \hat{m}_V^2)) , \\ m_W^2 &= \hat{m}_W^2 (1 - c_H^2 \xi^2) (1 + \mathcal{O}(\hat{m}_W^2 / \hat{m}_V^2)) . \end{aligned} \quad (1.13)$$

The parameter ξ can be either very small or of order unity. Both cases are realized in explicit models. While $\xi \ll 1$ is the most common situation, $\xi \sim 1$ only occurs in strongly coupled scenarios at very large g_V . In these approximations, SM tree-level experimental observation can be reproduced to percent accuracy.

Since $\hat{m}_W = \cos \theta_W \hat{m}_Z$, the W - Z mass ratio is thus given by

$$\frac{m_W^2}{m_Z^2} \simeq \cos^2 \theta_W . \quad (1.14)$$

Eq. (1.14) has one important implication on the masses of the new vectors. When combined with the custodial relation Eq. (1.11), it tells us that the charged and neutral V s are practically degenerate

$$M_\pm^2 = M_0^2(1 + \mathcal{O}(\%)) , \quad (1.15)$$

56 In the following, when working at the leading order in the limit Eq. (1.12), we can
 57 ignore the mass splitting and denote the mass of the charged and the neutral states
 58 collectively as M_V . It is easy to check that in that limit $M_V = \hat{m}_V$.

59 Decay Widths

Because of the hierarchy in the mass matrices, the mixing angles are naturally small. By looking at Eqs. (1.7), (1.9) and (1.12) we can estimate

$$\theta_{N,C} \simeq c_H \xi \frac{\hat{m}_{W,Z}}{\hat{m}_V} \leq 10^{-1} , \quad (1.16)$$

and after rotating to the mass basis, the coupling of the neutral and charged resonances to left- and right-handed fermion chiralities can be written in a compact form for each fermion species $F = \{l, q, 3\}$.

$$\begin{cases} g_L^N = \frac{g^2}{g_V} \frac{c_F}{2} \cos \theta_C + (g_L^Z)_{SM} \sin \theta_N \simeq \frac{g^2}{g_V} \frac{c_F}{2} , \\ g_R^N = (g_R^Z)_{SM} \sin \theta_N \simeq 0 \\ g_L^C = \frac{g^2}{g_V} \frac{c_F}{2} \cos \theta_C + (g_L^W)_{SM} \sin \theta_C \simeq \frac{g^2}{g_V} \frac{c_F}{2} , \\ g_R^C = 0 \end{cases} \quad (1.17)$$

In the above equation $(g_{L,R}^{W,Z})_{SM}$ denote the ordinary SM W and Z couplings (with the normalization given by $g_L^W = g/\sqrt{2}$).

Given that the rotation angles are small, the couplings further simplify, as also shown in the equation. We could see that V interact mainly with left-handed chiralities and that all the couplings for each fermion species are controlled by the parameter combination $g^2/g_V c_F$. This gives tight correlations among different channels

$$\Gamma_{V_{\pm} \rightarrow f \bar{f}'} \simeq 2\Gamma_{V_0 \rightarrow f \bar{f}'} \simeq N_C[f] \left(\frac{g^2 c_F}{g_V} \right)^2 \frac{M_V}{48\pi} , \quad (1.18)$$

where $N_C[f]$ is the number of colors (3 for the di-quark and 1 for the dilepton decays). The parameters $c_F = \{c_l, c_q, c_3\}$ control the relative BRs to leptons, light quarks and the third family.

In the case of di-boson decay width

$$\begin{aligned} \Gamma_{V_0 \rightarrow W_L^+ W_L^-} &\simeq \Gamma_{V_{\pm} \rightarrow W_L^{\pm} Z_L} \simeq \frac{g_V^2 c_H^2 M_V}{192\pi} \frac{(1 + c_H c_{VVV} \xi^2)^2}{(1 - c_H^2 \xi^2)^2} = \frac{g_V^2 c_H^2 M_V}{192\pi} [1 + \mathcal{O}(\xi^2)] , \\ \Gamma_{V_0 \rightarrow Z_L h} &\simeq \Gamma_{V_{\pm} \rightarrow W_L^{\pm} h} \simeq \frac{g_V^2 c_H^2 M_V}{192\pi} \frac{(1 - 4c_{VVHH} \xi^2)^2}{1 - c_H^2 \xi^2} = \frac{g_V^2 c_H^2 M_V}{192\pi} [1 + \mathcal{O}(\xi^2)] . \end{aligned} \quad (1.19)$$

60 Note that Eq. (1.19) is derived in the Equivalent Gauge [16] because the decay to
61 transverse SM vectors is highly suppressed while to the longitudinal parts grows with
62 the energy of the process, therefore the Unitary Gauge which is used in the original
63 Lagrangian is instead useful. The channels that are not shown in the above equations
64 are either forbidden or suppressed like the decays to transverse polarizations.

65 From this section, a very simple picture emerges. At small ξ , all the decay widths
66 are fixed with a given resonance mass M_V and the couplings $\{g^2 c_F/g_V, g_V c_H\}$ which
67 control the BRs in all relevant channels. Parameters c_{VVV} , c_{VVHH} and c_{VW} are
68 basically irrelevant. Thus, the basic phenomenology of this model is well described
69 by a good approximation.

70 1.2.3 Explicit Models

Now the general picture is clear, we can get exact values of the widths and BRs from explicit models. Consider two benchmark models, A and B, which correspond to two explicit models describing the heavy vectors in Refs. [17] and [12] respectively. All the c parameters are fixed to specific values in these models and the only free parameters are the resonance mass M_V and coupling g_V . Moreover, model A is inspired by weakly coupled extensions of the SM gauge group while model B is by strongly coupled scenarios of EWSB, *i.e.* Composite Higgs models, we will consider them in different regions of g_V , relatively small $g_V \leq 3$ and relatively large $g_V \geq 3$.

Figure 1-1 shows the BRs as functions of the mass in model A and B. As expected from the previous discussion and according to Refs. [17], model A predicts

$$\begin{aligned} c_H &= -g^2/g_V^2, \quad c_F \simeq 1, \\ |g_V c_H| &\simeq g^2 c_F / g_V \simeq g^2 / g_V. \end{aligned} \quad (1.20)$$

Therefore Eq. (1.18) and (1.19) can be determined in the following form for V_0 in model A ($g_V = 1$),

$$\begin{aligned} \Gamma_{V_0 \rightarrow f \bar{f}'} &\simeq N_c[f] \frac{g^4 M_V}{96\pi} \\ \Gamma_{V_0 \rightarrow W^+ W^-} &\simeq \Gamma_{V_0 \rightarrow Z h} \simeq \frac{g^4 M_V}{192\pi}. \end{aligned} \quad (1.21)$$

One can easily check either from the plot or the equation, a factor of two difference comparing the BRs between fermions and bosons. Due to the color factor, leptons and quarks also have a difference by a factor of three. Since the c_F term is universal both in A and B. The total width in model A decreases with increasing g_V because of the overall suppression (g^2/g_V) in Eq. (1.20).

On the contrary, in model B the c_H term is unsuppressed

$$\begin{aligned} c_H &\simeq c_F \simeq 1 , \\ g_V c_H &\simeq -g_V , \quad g^2 c_{c_F} / g_{g_V} \simeq g^2 / g_V . \end{aligned} \tag{1.22}$$

Thus the determinate V_0 decay widths for model B ($g_V = 3$) are

$$\begin{aligned} \Gamma_{V_0 \rightarrow f \bar{f}} &\simeq N_c[f] \frac{g^4 M_V}{342\pi} \\ \Gamma_{V_0 \rightarrow W^+ W^-} &\simeq \Gamma_{V_0 \rightarrow Z h} \simeq \frac{3M_V}{64\pi} . \end{aligned} \tag{1.23}$$

71 For model B _{$g_V=3$} the dominant BRs are into di-bosons and the fermionic decays are
 72 extremely suppressed. Moreover, the total width increases with increasing g_V since it
 73 is dominated by the di-boson width which grows with g_V as expected from Eq. (1.22).
 74 This model B is particularly interesting for the present search, since it predicts signal
 75 cross sections in order of fb [15] [18] [Fig. 1-2], branching ratios to vector bosons close
 76 to unity, and thus being accessible at the LHC. In the latter chapters, the mass eigen-
 77 state of the neutral heavy vector boson in model B scenario refers to the Z' particle,
 78 which is the search target of this thesis.

79

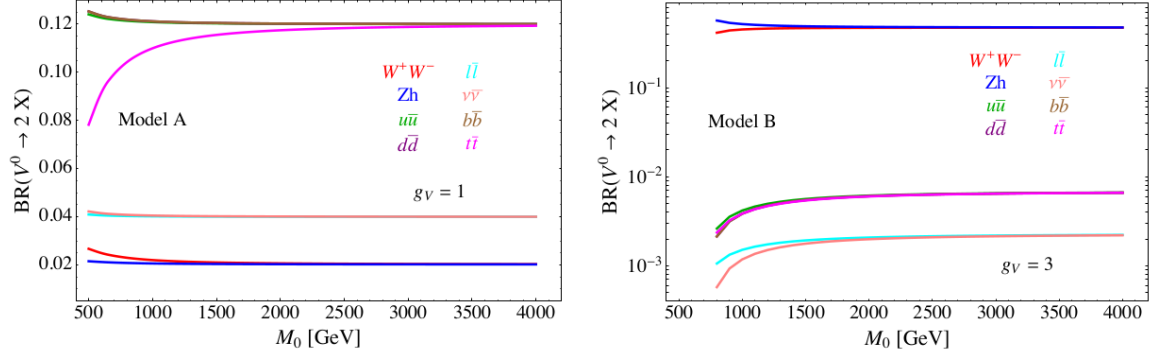


Figure 1-1: Branching ratios as a function of the resonance mass for the HVT benchmark model A(left) and model B(right).

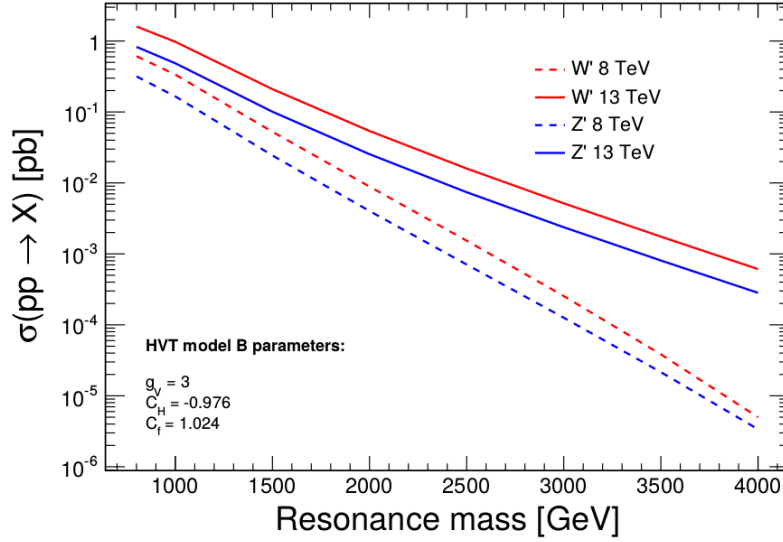


Figure 1-2: Theoretical production cross-section as a function of new resonance particles for HVT model B benchmark. Dash lines are 8 TeV predictions while solid lines are 13 TeV predictions.

Chapter 2

CMS detector and LHC

This thesis is done via analyzing the data collected by the Compact Muon Solenoid (CMS) detector at the Large Hadron Collider (LHC). CMS is one of the two largest detectors built on the LHC. This chapter will briefly introduce the LHC and the CMS detector.

2.1 Large Hadron Collider

The LHC is the world's most powerful hadron collider and the largest experimental facility ever. It was built by the European Organization for Nuclear Research (CERN) between 1998 and 2008 in collaboration with over 10,000 scientists and engineers from over 100 countries, as well as hundreds of universities and laboratories. It lies in a tunnel 27 km in circumference, as deep as 175 m beneath the France–Switzerland border near Geneva. The designed maximum collision energy and highest luminosity of the LHC are 14 TeV and $10^{-34}\text{cm}^{-2}\text{s}^{-1}$ respectively.

Other accelerators that had been originally built at CERN for previous experiments is working as an injection chain for the LHC now. The proton beam starts from LINAC, a small linear accelerator, where its energy firstly reaches 50 MeV. It then passes through a booster and goes to the PS, where it is accelerated up to 25 GeV. After that, it reaches 450 GeV in the SPS. The beam is finally injected in the LHC ring from the SPS, it is accelerated up to 4 TeV in 2012. In early 2015, the

100 proton beam had been accelerated to 6.5 TeV, a value near its designed energy, before
101 undergoing collision.

102 There are four collision points at the LHC, corresponding to four main experi-
103 ments, CMS, ATLAS, LHCb and ALICE. The ALICE experiment is optimized to
104 study heavy-ion (Pb-Pb nuclei) collisions and focusing on the physics of strongly
105 interacting matter at extreme energy densities. LHCb is a specialized b-physics ex-
106 periment, measuring the parameters of CP violation in the interactions of b-hadrons.
107 Such studies can help to explain the matter-antimatter asymmetry of the universe.
108 Last, CMS and ATLAS are two general purpose detectors. The aims of these two
109 experiments are investigating a wide range of physics, including the search for the
110 beyond standard model particles, extra dimensions, and dark matter.



Figure 2-1: Overview of the LHC and relative location of the detectors.

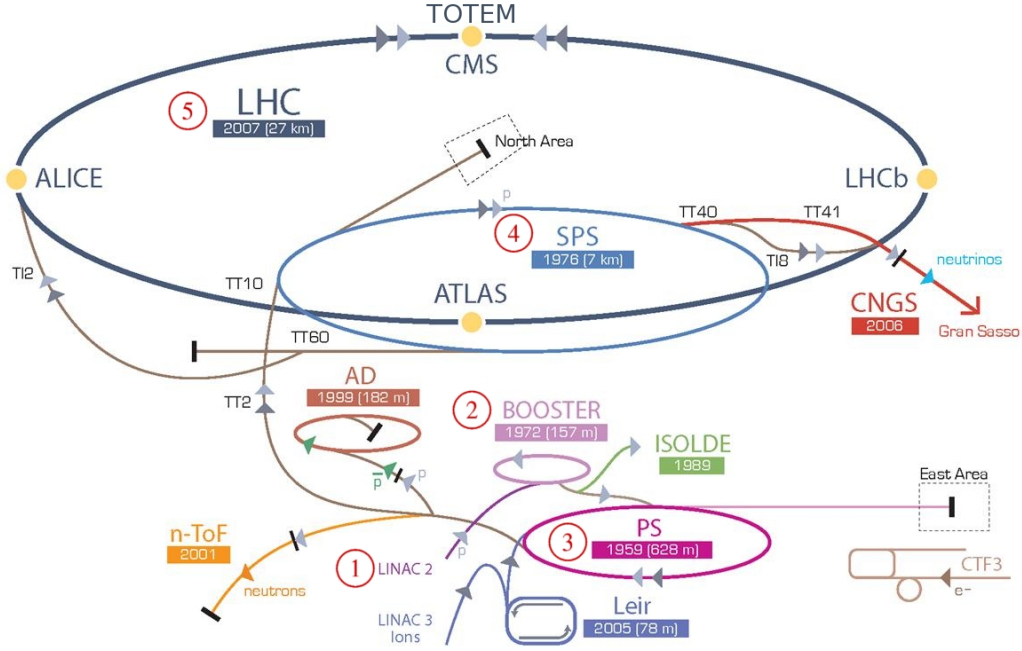


Figure 2-2: CERN accelerator complex.

2.2 Compact Muon Solenoid

The Compact Muon Solenoid (CMS) detector is designed to cope very high rate of interactions expected to take place at the high LHC luminosity. It has the typical structure of detectors at hadron colliders: a central region (*barrel*) enclosed by two disks (*endcaps*). The structure of CMS can be seen in Fig. (2-3).

Solenoid and Sub-detectors

CMS features a powerful superconducting coil, generating a solenoidal magnetic field around 3.8 Tesla in a large volume, which hosts different sub-detectors. The magnetic field lines close through steel yoke in the outer region and the distinct sub-detectors are designed in order to obtain the highest possible resolution and the largest acceptance for every kind of particles.

The innermost layer is a silicon-based tracker. Surrounding it is a scintillating crystal electromagnetic calorimeter (ECAL), which is itself surrounded with a sampling calorimeter for hadrons (HCAL). The tracker and the calorimeters are compact

125 enough to fit inside the CMS Solenoid. Outside the magnet are the large muon
 126 detectors separated by layers of the steel yoke.

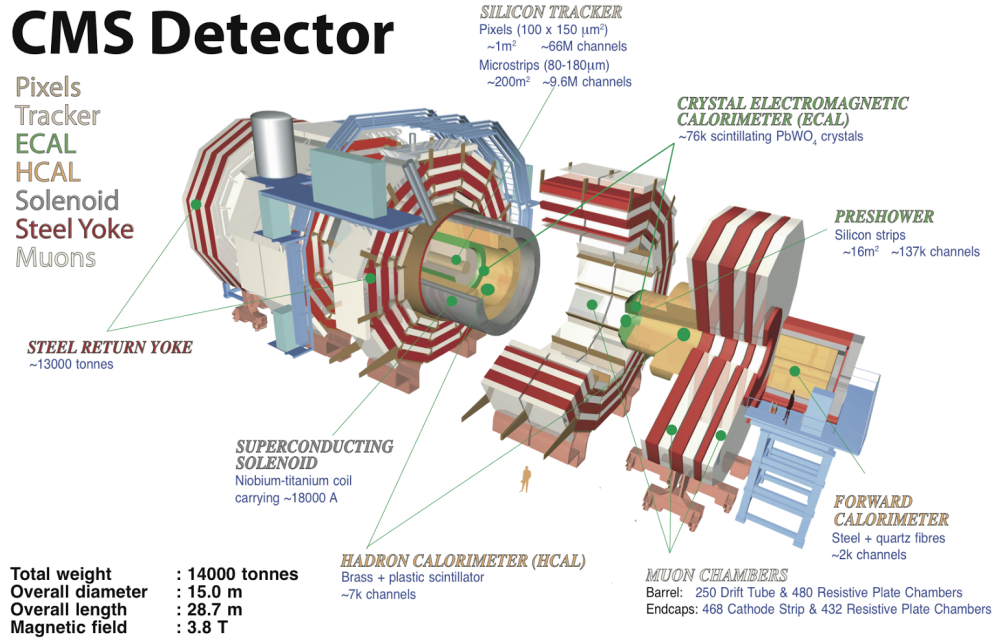


Figure 2-3: Structure overview of the CMS detector.

127 Coordinate System

128 The CMS coordinate system is oriented such that the x -axis points to the center of
 129 the LHC ring, the y -axis points vertically upward and the z -axis is in the direction
 130 of the beam. The azimuthal angle ϕ is measured from the x -axis in the xy plane and
 131 the radial coordinate in this plane is denoted by r . The polar angle θ is defined in the
 132 rz plane, while the pseudo-rapidity $\eta = -\ln \tan(\theta/2)$. The momentum component
 133 transverse to the beam direction, denoted by p_T , is computed from the x - and y -
 134 components, and the transverse energy is defined as $E_T = E \sin \theta$.

2.2.1 Tracker

Tracker is the most inner part of CMS that contacts the productions of collisions in the first place. It traces the charged particles' trajectories without considering their energy as possible. Physicists can reconstruct the vertices of the interaction and the momentum of charged particles by linking tracks to the collider's pipe and measuring the curves of particles under magnetic field.

The tracking system is composed of two kinds of detector, the pixel detector and silicon strip detector. The pixel detector is built from three barrel layers at $r=44, 73, 102$ mm, and two endcap disks on each side at $z=\pm 345, \pm 465$ mm.

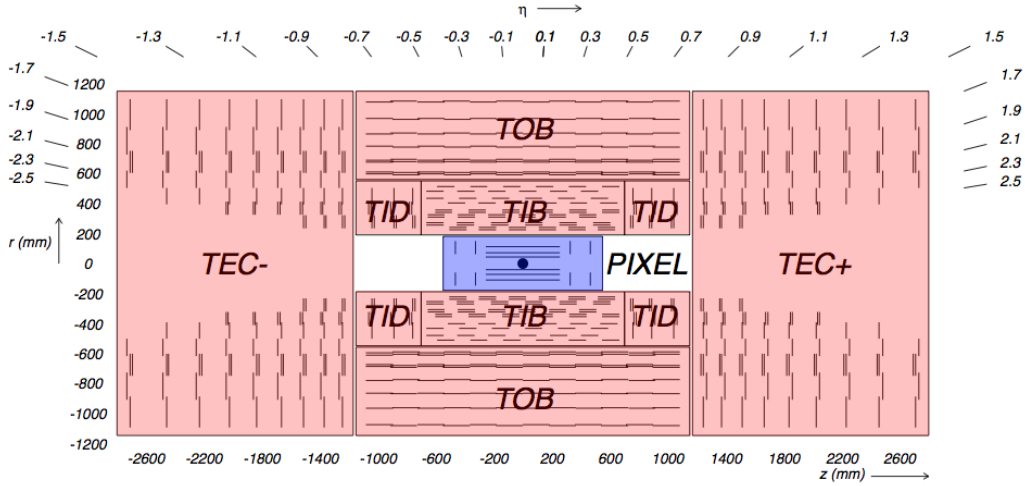


Figure 2-4: Schematic layout of tracker.

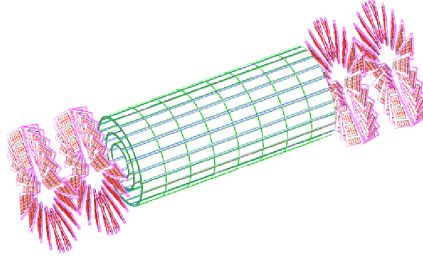


Figure 2-5: The pixel detector inside tracker.

And the pixel detector consists of 1440 segmented silicon sensor modules with total 66 million readout channels. Charge carriers are distributed over several pixels.

146 The analog pulse height information can be used to calculate the center of certain
 147 charge distribution which could improve the hit information. The spatial resolution
 148 is measured to be about $10\ \mu m$ for the $r - \phi$ plane or about $20\ \mu m$ for z direction
 149 measurement.

150 Outside the pixel detector, there comes the silicon strip detector. The barrel region
 151 of silicon strip detector is divided into two parts, the Tracker Inner Barrel (TIB) and
 152 the Tracker Outer Barrel (TOB). The former is composed of four layers of silicon
 153 sensors with a thickness of $320\ \mu m$ and of strip pitches varying from 80 to $120\ \mu m$.
 154 The TOB is made of six layers. In this sub-detector thicker silicon sensors ($500\ \mu m$)
 155 are employed, while the strip pitch varies from 120 to $180\ \mu m$. The endcap region
 156 ($|\eta| > 1.6$) is covered by the Tracker Inner Disks (TID) and the Tracker End Cap
 157 (TEC). The entire silicon strip detector is comprised of 15200 high-sensitivity modules
 158 consisting of detecting unit, supporting structure and readout electronic system.

159 **2.2.2 ECAL**

160 The Electromagnetic Calorimeter (ECAL) measures the energy of photons, electrons
 161 and positrons. It is placed just outside the tracker, but still inside the solenoid.
 162 ECAL is made of 74848 lead-tungstate ($PbWO_4$) crystals. This material is charac-
 163 terized by a high density ($8.28\ g/cm^3$), which gives the crystals a very compact form
 164 and makes them particularly suitable to be placed inside the magnetic coil. Another
 165 reason, this material has also a fast temporal response ($\sim 10\ ns$) and its radiation
 166 length (X_0) of $0.89\ cm$ give ECAL the possibility to fully contain the expansion of
 167 the electromagnetic shower.

168 The arrangement of ECAL is shown in Fig. (2-6). The barrel crystals have a front
 169 face area of $2.2 \times 2.2\ cm^2$ and a length of $23\ cm$. They are positioned at $r = 1.29\ m$
 170 in pseudo-rapidity region $0 < |\eta| < 1.479$. The crystals in the endcaps have a
 171 $2.47 \times 2.47\ cm^2$ front face, a $22\ cm$ length and they are positioned at $z = 3.17\ m$ in
 172 $1.479 < |\eta| < 3.0$. A Preshower detector is placed in front of the endcaps crystals.
 173 The active elements of Preshower are two planes of silicon strips with a pitch of $1.9\ mm$,
 174 which lie behind disks of lead absorber at depths of $2X_0$ and $3X_0$. It allows the

rejection of photon pairs from π^0 decays and improve the estimation of the direction of photons, to enhance the measurement of the two-photon invariant mass.

The energy resolution of the ECAL is given by three different contributions [19],

$$\frac{\sigma_E}{E} = \frac{a}{\sqrt{E}} \oplus \frac{b}{E} \oplus c \quad (2.1)$$

where the first term is statistical in nature, it also contains fluctuation in showering and in the amplification through photodiodes ($a \sim 2.8\%$), the second one considers electronic noise and pile-up ($b \sim 12\%$) and the last term is mainly due to the calibration ($c \sim 0.3\%$).

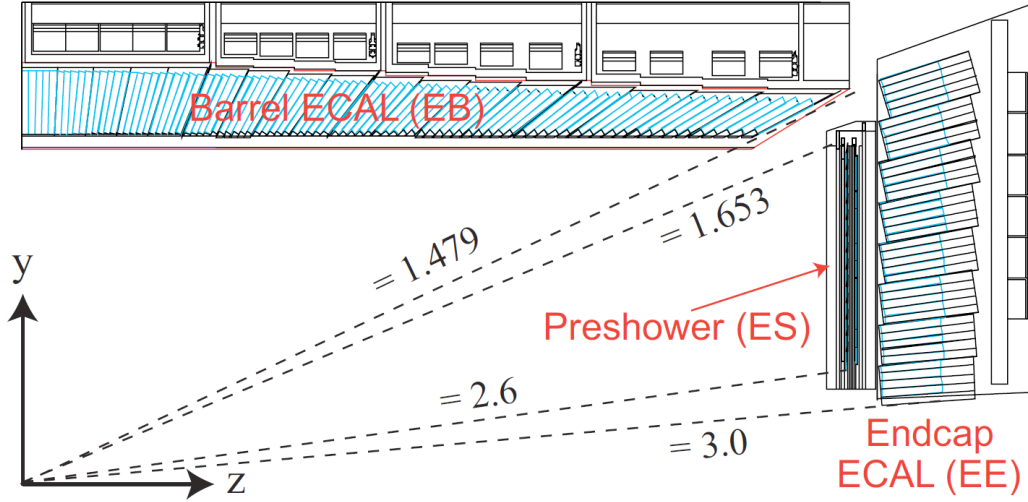


Figure 2-6: Schematic layout of the CMS ECAL.

2.2.3 HCAL

2.2.4 Muon Chamber

2.2.5 Trigger System

Bibliography

- [1] ATLAS Collaboration. Observation of a new particle in the search for the Standard Model Higgs boson with the ATLAS detector at the LHC. *Phy. Lett. B*, 716:1, 2012.
- [2] CMS Collaboration. Observation of a new boson at a mass of 125 GeV with the CMS experiment at the LHC. *Phy. Lett. B*, 716:30, 2012.
- [3] CMS Collaboration. Observation of a new boson with mass near 125 GeV in pp collisions at $\sqrt{s} = 7$ and 8 TeV. *JHEP*, 06:081, 2013.
- [4] CMS Collaboration. Precise determination of the mass of the Higgs boson and tests of compatibility of its couplings with the standard model predictions using proton collisions at 7 and 8 TeV. *Eur. Phys. J. C*, 75:212, 2015.
- [5] ATLAS Collaboration. Measurement of the Higgs boson mass from the $H \rightarrow \gamma\gamma$ and $H \rightarrow ZZ^* \rightarrow 4l$ channels in pp collisions at center-of-mass energies of 7 and 8 TeV with the ATLAS detector. *Phys. Rev. D*, 90:052004, 2014.
- [6] ATLAS Collaboration. Evidence for the spin-0 nature of the Higgs boson using ATLAS data. *Phys. Lett. B*, 726:120, 2013.
- [7] CMS and ATLAS Collaboration. Combined Measurement of the Higgs Boson Mass in pp Collisions at $\sqrt{s} = 7$ and 8 TeV with the ATLAS and CMS Experiments. *Phys. Rev. Lett.*, 114:191803, 2015.
- [8] Mads T. Frandsen. Minimal Walking Technicolor. arXiv:0710.4333 [hep-ph], <http://arxiv.org/abs/0710.4333>, 2007.
- [9] B. McElrath T. Han, H. E. Logan and L.-T. Wang. Phenomenology of the little Higgs model. *Phys. Rev. D*, 67:095004, 2003.
- [10] M. Schmaltz and D. Tucker-Smith. LITTLE HIGGS THEORIES. *Annual Review of Nuclear and Particle Science*, 55:no. 1, 229–270, 2005.
- [11] M. Perelstein. Little Higgs models and their phenomenolog. *Progress in Particle and Nuclear Physics*, 58:no. 1, 247–291, 2007.
- [12] D. Marzocca R. Contino, D. Pappadopulo and R. Rattazzi. On the effect of resonances in composite Higgs phenomenology. *Journal of High Energy Physic*, 2011:no. 10, 1–50, 2011.

- 214 [13] M. Serone D. Marzocca and J. Shu. General composite Higgs model. *Journal of*
215 *High Energy Physics*, 2012:no. 8, 1–52, 2012.
- 216 [14] C. Cski B. Bellazzini and J. Serra. Composite Higgses. *Eur. Phys. J.*, C74:no.
217 5, 2766, 2014.
- 218 [15] R. Torre D. Pappadopulo, A. Thamm and A. Wulzer. Heavy vector triplets:
219 bridging theory and data. *Journal of High Energy Physics*, 2014:no. 9, 1–50,
220 2014.
- 221 [16] Andrea Wulzer. An Equivalent Gauge and the Equivalence Theorem.
222 arXiv:1309.6055 [hep-ph], <http://arxiv.org/abs/1309.6055>, 2013.
- 223 [17] W.-Y. Keung V. Barger and E. Ma. Gauge model with light W and Z bosons.
224 *Phys. Rev. D*, 22:727, 1980.
- 225 [18] Lisa Benato, Yu-Hsiang Chang, Ching-Wei Chen, Michele de Gruttola, Ra-
226 man Khurana Ji-Kong Huang, Stefano Lacaprara, Yun-Ju Lu, Jacopo Pazzini,
227 Maurizio Pierini, Henry Yee-Shian Tong, Jun-Yi Wu, Shin-Shan Eiko Yu, Marco
228 Zanetti, and Alberto Zucchetta. Search for heavy resonances decaying into a vec-
229 tor boson and a higgs boson in the $(ll, l\nu, \nu\nu)b\bar{b}$ final state. CMS Note 2015/186,
230 CMS, 2015.
- 231 [19] A Benaglia. The CMS ECAL performance with examples. *JINST*, 09:C02008,
232 2014.